IEEE Photonics Journal
An IEEE Photonics Society Publication

Open Access

Microcavity Effect in InAs/GaAs Quantum Dot Infrared Photodetector on a Si Substrate Fabricated With Metal Wafer Bonding and Epitaxial Lift-Off Techniques

Volume 11, Number 1, February 2019

Ho Sung Kim
G. H. Ryu
S. Y. Ahn
H. Y. Ryu
W. J. Choi

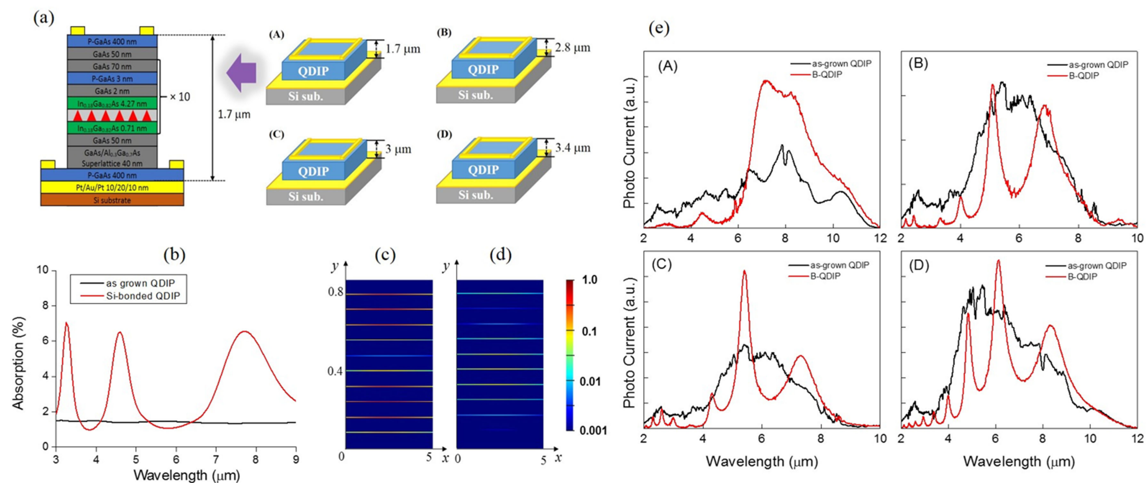

DOI: 10.1109/JPHOT.2018.2890724
1943-0655 © 2018 IEEE

IEEE photonics SOCIETY
IEEE

Microcavity Effect in InAs/GaAs Quantum Dot Infrared Photodetector on a Si Substrate Fabricated With Metal Wafer Bonding and Epitaxial Lift-Off Techniques

Ho Sung Kim,[1,3] G. H. Ryu,[1,2] S. Y. Ahn,[1] H. Y. Ryu,[2] and W. J. Choi[1]

[1]Center for Opto-Electronics Materials and Devices, Korea Institute of Science and Technology, Seoul 02792, South Korea
[2]Department of Physics, Inha University, Incheon 22212, South Korea
[3]Department of Electrical and Computer Engineering, University of Waterloo, Waterloo, ON N2L 3G1, Canada

DOI:10.1109/JPHOT.2018.2890724
1943-0655 © 2018 IEEE. Translations and content mining are permitted for academic research only. Personal use is also permitted, but republication/redistribution requires IEEE permission. See http://www.ieee.org/publications_standards/publications/rights/index.html for more information.

Manuscript received December 1, 2018; revised December 24, 2018; accepted December 28, 2018. Date of publication January 9, 2019; date of current version January 15, 2019. This work was supported in part by the KIST Institutional Program of Flag-Ship (2E28180) and in part by the Pioneer Research Center Program through the National Research Foundation of Korea funded by the Ministry of Science, ICT & Future Planning (2014M3C1A3052580). Corresponding authors H. Y. Ryu and W. J. Choi (e-mail: hanryu@inha.ac.kr; wjchoi@kist.re.kr).

Abstract: In this paper, the microcavity effect in quantum dot infrared photodetectors (QDIPs) on a Si substrate, fabricated by means of metal wafer bonding (MWB) and epitaxial lift-off (ELO) processes, was demonstrated by comparing the photocurrent spectrum and the simulated absorption spectrum. Four QDIPs having a different cavity length of 1.7, 2.8, 3, and 3.4 μm were fabricated and compared with simulation based on the finite-difference time-domain method. The resonance peaks were observed in both photocurrent spectrum and absorption spectrum due to the microcavity formed by the bottom mirror of Pt/Au layer and the flat GaAs/air interface. The peak wavelength of the photocurrent spectrum in all four QDIPs on Si samples shows a good agreement with the simulated absorption spectrum. The bias-dependent photocurrent was also measured to study the microcavity effects more in depth. The ratio of the increased photocurrent under bias condition shows higher value in the microcavity QDIPs, showing that the microcavity contributes to generate photocurrent effectively. From these results, we believe that the MWB and ELO could be useful to make the microcavity in many integrated chemical and biosensing application.

Index Terms: Quantum dot infrared photodetector, microcavity, metal wafer bonding, epitaxial lift-off.

1. Introduction

Integration of III–V semiconductors on Si substrate has been widely studied due to the possibility of low cost fabrication using Si substrate and excellent opto-electronic conversion efficiency of III–V material for opto-electronic devices [1]–[3]. A direct growth of III–V materials on a Si substrate in molecular beam epitaxy (MBE) or molecular organic chemical vacuum deposition (MOCVD) and a wafer bonding of III–V materials on a Si substrate are studied for the integration of III–V on Si substrate. The direct growth of III–V materials on a Si substrate can reduce the fabrication steps and

be produced by a large scale [4]–[7]. However, it is difficult to make the high quality of III–V layers on Si substrate, compare to that grown on lattice matched III–V substrates. On the other hand, the wafer bonding technology can be achieved on any substrate whose surface is atomically flat. Most of all, the material characteristics do not change after the wafer bonding process and epitaxial lift-off (ELO) [8]–[11]. Metal wafer bonding (MWB) has an advantage of using a very thin gold layer of $\sim$20 nm, relying on the Van-der-Waals force, as compared to gold metal eutectic bonding which needs a thick gold layer of more than 200 nm. The ELO process has an advantage of skipping the chemical mechanical process (CMP) to remove the substrate.

Recently, quantum-well infrared photodetectors (QWIPs) and quantum-dot infrared photodetectors (QDIPs) have been actively studied using the microcavity structure to increase light absorption and quantum efficiency [12]–[17]. The enhanced performances of the QWIPs and QDIPs with the microcavity structure were reported by using distributed Bragg reflector (DBR) [12]–[14] or double-sided thick gold metals [15]–[17]. Usually, the DBR layer is formed by depositing the GaAs and the AlAs layer alternately. However, a very thick DBR is needed to obtain high reflectivity for the particular wavelength of light. With respect to the double-sided thick gold metals, this process uses gold eutectic bonding which needs high temperature to bond and CMP to etch the substrate. These methods make the sample growth and the device fabrication difficult. In this paper, we demonstrate the microcavity QDIP structure on Si substrate (B-QDIP) using MWB and ELO processes instead of using the DBR or double-side gold metals.

In our previous study, QDIPs on a Si substrate were fabricated successfully by means of MWB and ELO technologies [18]. According to our studies, B-QDIP showed the change of photoluminescence (PL) characteristics as well as the change of the spectral response of the device. It was revealed that the PL change was attributed to the cavity effect of the backside mirror of Pt/Au (bonding material) and the front side facet of GaAs/air. However, the cavity effect in the mid-infrared (MIR) spectrum of the QDIP has not been clearly demonstrated. To observe this, it was necessary to measure the reflectance of the B-QDIP in MIR wavelength region. However, it was impossible to measure the exact reflectance because the beam spot size (1 μm^2) of the MIR source was larger than the device size of the B-QDIP (800 μm^2) which had been fabricated using ultra-fast ELO technology [9]. Moreover, it was also quite challenging to obtain the reflectance of the thin bonding metal in the MIR region at cryogenic temperature. Therefore, a different approach should be taken to demonstrate the cavity effect in the MIR region.

In this work, we verify that the spectral response change of the B-QDIP originates from the microcavity effect by comparing the simulation and the experimental results of the B-QDIP devices on Si substrate. B-QDIPs with different cavity length are grown and fabricated to investigate the dependence of spectral response change on the cavity length. The absorption spectrum is calculated using finite-difference time-domain (FDTD) simulation for the corresponding structures. In this way, we find the origin of the spectral response change and show the microcavity structure in the QDIPs on Si with MWB and ELO processes. Finally, we investigate the effect of microcavity in more depth by measuring the bias-dependent photocurrent (PC) spectrum.

2. Experiment and Simulation

2.1 Device Fabrication

The four QDIP devices were grown by molecular beam epitaxy (MBE) and the detector samples have the cavity length of 1.7 μm (A), 2.8 μm (B), 3 μm (C), and 3.4 μm (D), respectively. The schematic diagram of the B-QDIP structures is depicted in Fig. 1. The p-i-p QDIP structure was grown on a semi-insulating GaAs (100) substrate. The p-i-p QDIPs consisted of p+ GaAs contact layers, 75 nm spacer GaAs layers with a 3-nm-thick p-type modulation doped GaAs layer and a dot-in-a-well (DWELL) structure. In the DWELL active layer, 1.8 monolayer of InAs QDs, grown with the Stranski-Krastanov growth mode at 480 °C, were sandwiched between a 7.1 Å of $In_{0.18}Ga_{0.82}As$ layer and a 42.7 Å of $In_{0.18}Ga_{0.82}As$ layer. The AlAs sacrificial layer was included in the growth of QDIP structure for the future ELO processing step. After epitaxial growth, Pt/Au (10/10 nm) was

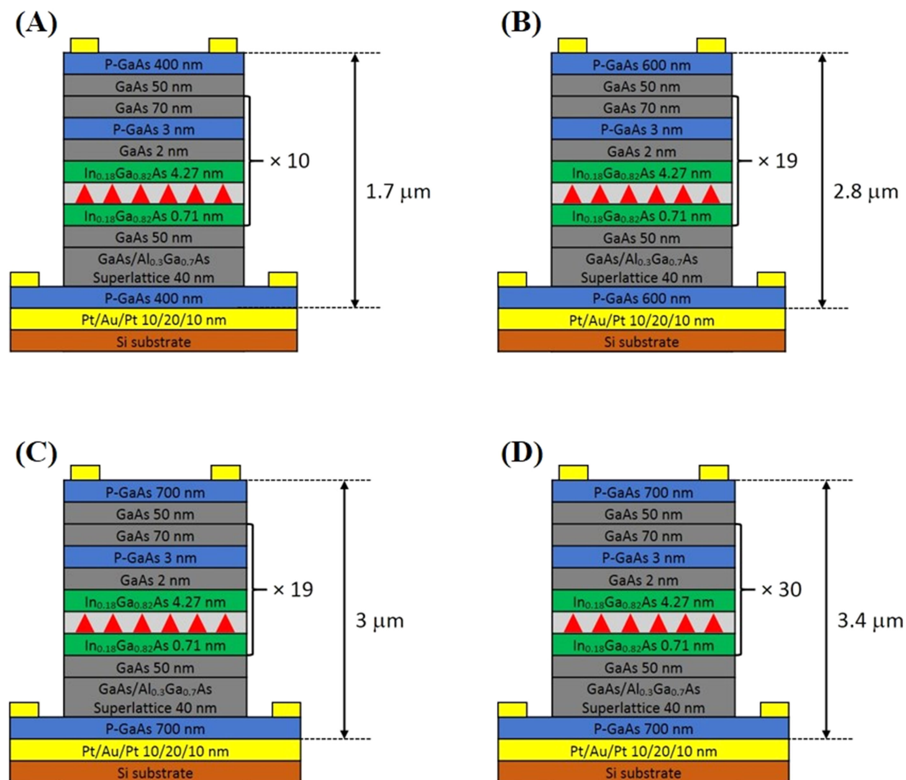

Fig. 1. The schematic diagram of the B-QDIP samples. Samples A, B, C and D has cavity length of 1.7 μm, 2.8 μm, 3 μm and 3.4 μm, respectively.

deposited onto both the QDIPs and Si substrates as a bonding material. The bonding was done by pressing two wafers together at room temperature. In the ELO step, the AlAs layer was selectively etched away by dipping the HF and aceton one to one solution and the GaAs wafer was lifted-off. The detailed growth and fabrication processes are described in reference [18]. Finally, the device was completed, followed by mesa etching and metallization. The different optical cavities were grown by changing a repetition number of cycle of active layers. For close comparison of the related structure, two devices, which are B and C, have different contact layer thickness only, which means these devices have a same thickness of the active layer. All device samples have the same device size of 800 μm^2. They were fabricated in simultaneous processes and measured under the same condition. The PC spectrum of each QDIP device was measured at 77 K using Fourier transform infrared spectrometer (FTIR). In this FTIR system, a global source emitting MIR radiation along with a KBr beam splitter was used. Signals were amplified by a low-noise current amplifier (Keithley 428) and then embedded in the spectrometer. PC signals at zero voltage bias were compared with the calculated absorption results and were measured at various bias voltages to observe the microcavity effects.

2.2 Simulation

The absorption characteristics of fabricated QDIP devices were numerically investigated using an FDTD method with a perfectly-matched layer boundary condition. A commercial software, FDTD Solutions by Lumerical Inc., was employed for the simulations [19]. A planewave source was incident on the top surface of the QDIP device, and the power absorbed at the QD layers was calculated in the wavelength range from 3 to 9 μm. In the simulation, the material dispersion of GaAs, DWELL layers, and Pt/Au layers was also taken into consideration. In the FDTD simulation, the absorbed

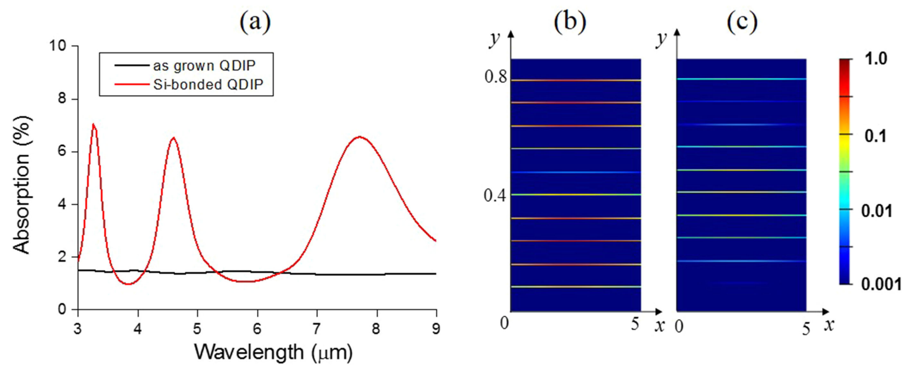

Fig. 2. (a) Simulated absorption spectra for as-grown QDIP and B-QDIP sample A. The distribution of electric field intensity in QD layers is shown at the wavelength of (b) 3.2 μm and (c) 3.9 μm. A color bar representing relative intensity is shown on the right of figures.

power was calculated according to the following formula [15].

$$P_{abs} = -0.5w|E|^2 \text{imag}(e) \quad (1)$$

where ω, E, and ε is angular frequency, electric field, and permittivity. Therefore, the power absorption can be simply calculated using the electric field intensity and the imaginary part of the permittivity at QD absorbing layers.

In the FDTD simulation, each DWELL active region was assumed to be a 5-nm-thick single plane layer. Since the total thickness of the DWELL region is much shorter than the light wavelength, detail information on layer structures and QD shapes of the DWELL is not necessary in the FDTD simulation. The absorption coefficient of the QD layers was assumed to be 10^4 cm^{-1} at the wavelength of 6 μm according to Ref. [20]–[22]. Although the absolute value of absorption is influenced by the absorption coefficient, the relative absorption enhancement, which is the ratio of the absorption of the B-QDIP to that of as-grown QDIP, was found to be almost unchanged with the choice of the absorption coefficient.

Fig. 2 shows the simulated results for B-QDIP sample A with the cavity length of 1.7 μm. The absorption spectrum of the B-QDIP sample shows several resonance peaks as a result of the cavity-enhanced light absorption, whereas that of the as-grown sample shows nearly constant absorption in the simulated wavelength range. Fig. 2(b) and (c) shows the distribution of electric field intensity in QD absorbing layers at the wavelength of 3.2 and 3.9 μm, respectively. At 3.2 μm, where an absorption peak exists, strong absorption from the resonant standing wave pattern is observed at QD layers. However, relatively weak absorption is observed at 3.9 μm, which corresponds to anti-resonant condition. The simulated absorption spectra will be compared and discussed in the next section.

3. Results and Discussion

Fig. 3 shows the PC response of the as-grown QDIP and the B-QDIP. The black and red lines indicate the photocurrent signal of the as-grown QDIP detector and the B-QDIP, respectively. The spectral shape of the as-grown samples B and C looks quite similar because the number of QD active layers is the same for samples B and C. On the contrary, the as-grown samples A, B, and D show different spectral shape which results from the difference in the number of active layers between samples A, B, and D. For all samples from A to D, the PC spectrum of the B-QDIP changes greatly from that of the as-grown QDIP. There exist resonant peaks in the spectrum for the B-QDIP samples and the number of peaks increases as the cavity length increases. This phenomenon can be easily understood from the optical cavity effect. In the optical cavity comprised of two plane mirrors, the resonance wavelength is proportional to the cavity length.

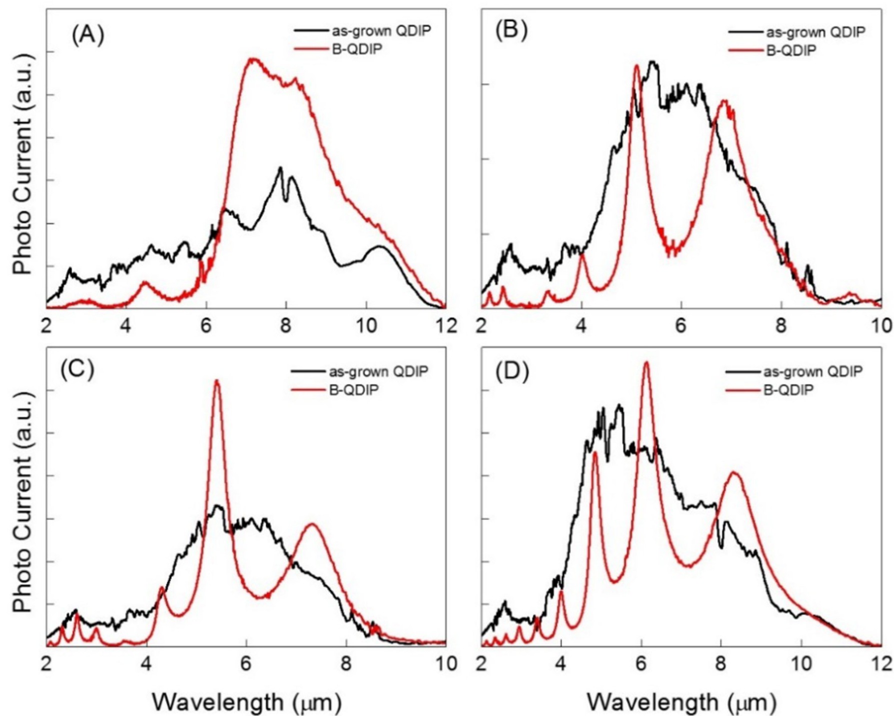

Fig. 3. The photo-current response of the as-grown QDIP and the B-QDIP. Each spectrum (A), (B), (C), and (D) corresponds to the sample with cavity length of 1.7 μm (sample A), 2.8 μm (sample B), 3 μm (sample C), and 3.4 μm (sample D), respectively.

Fig. 4 shows the relative enhancement of PC which is obtained by dividing the PC spectrum of the B-QDIP by that of the as-grown QDIP. Several successive peaks arising from the resonant cavity enhanced photo current are observed from all B-QDIP samples. This feature clearly shows the characteristics of microcavity effect in B-QDIP structures. When samples B and C are compared closely, the redshift of peak wavelengths is observed as the cavity length increases, though they have a same active layer thickness. In addition, the intensity of relative enhanced PC of sample C at the 3rd and the 4th peaks is increased compared to that of sample B. This changed PC spectra of samples B and C directly indicate the microcavity effects in the QDIP on Si fabricated using the MWB and ELO method, resulting in the resonant cavity enhanced photo-current. To find out the origin of the microcavity effect in B-QDIP, the absorption spectrum was calculated and compared.

Fig. 5 shows the simulated relative absorption enhancement spectrum of each sample. Here, the relative absorption enhancement is obtained by dividing the absorption spectrum of the B-QDIP by that of the as-grown QDIP. The absorption spectra of all B-QDIP samples show several resonant absorption peaks, and the number of peaks increases as the cavity length increases, which is consistent with the experimental results in Fig. 3. This resonant feature arises from the microcavity structure formed between the Pt/Au bonding layer and the flat GaAs/air interface. The simulated relative absorption enhancement is somewhat larger than the measured relative PC enhancement. This is because the capture probability of an electron was not considered in FDTD simulations, resulting in the discrepancy between the simulation and experiment results. The PC is a function of the escape probability for an excited electron and the capture probability. This means that the intensity of the relative enhancement cannot be directly compared between the absorption and the PC.

The peak wavelength of the measured PC spectrum in Fig. 3 and the simulated relative absorption spectrum in Fig. 5 are compared. Fig. 6 shows the peak wavelength for each peak number of

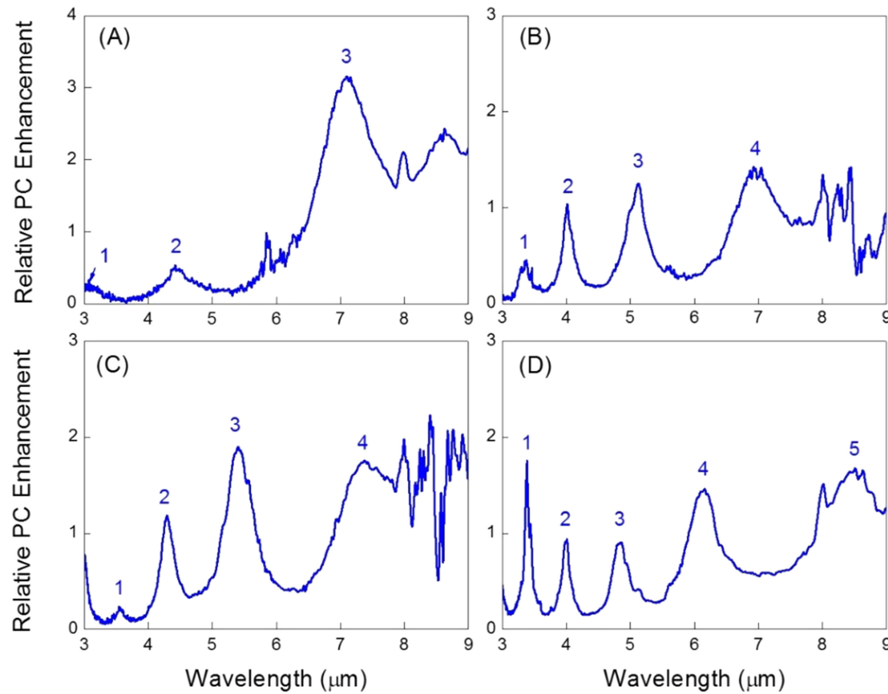

Fig. 4. The relative enhancement of the photo-current spectrum for the samples A, B, C, and D. The relative enhancement refer to the ratio of the photocurrent of the B-QDIP to that of the as-grown QDIP.

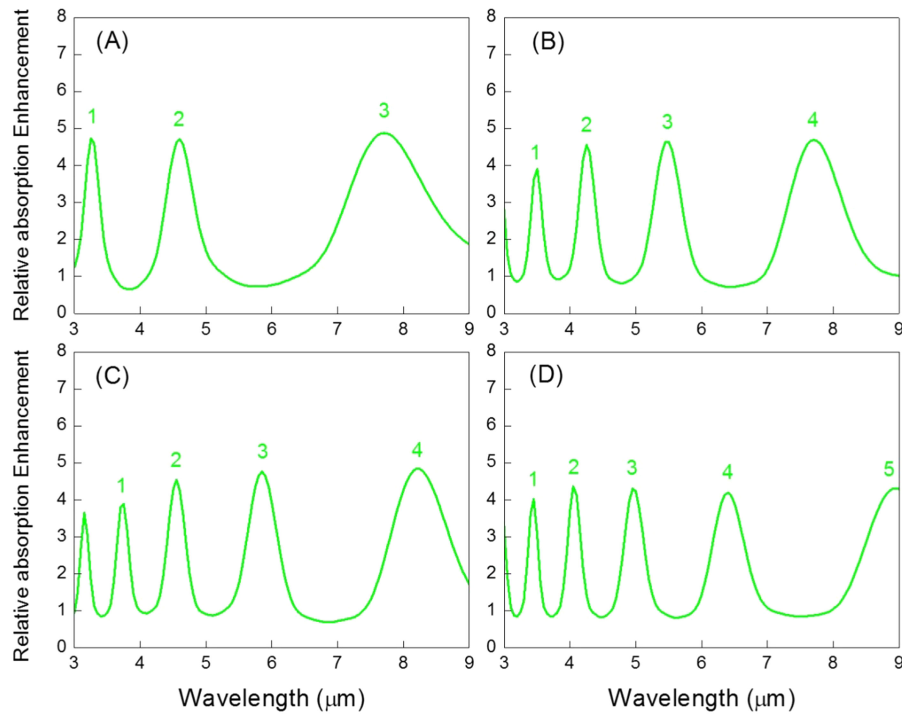

Fig. 5. The simulated relative absorption spectrum for the samples A, B, C, and D. The relative absorption refer to the ratio of the absorption of the B-QDIP to that of the as-grown QDIP.

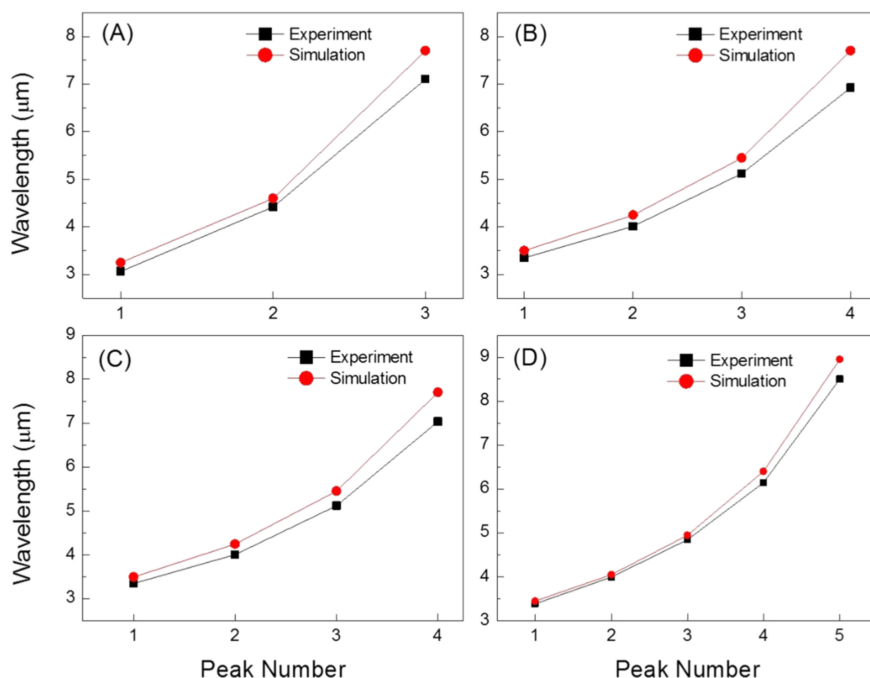

Fig. 6. The comparison of the experimentally measured peak wavelength of B-QDIP and the calculated peak absorption wavelength of B-QDIP for samples A, B, C, and D.

the measured relative PC spectrum and the simulated absorption spectrum. In general, the peak wavelength of the relative PC and absorption spectrum shows a reasonably good agreement in all four samples. In all cases, the simulated peak wavelength is slightly higher than the measured peak wavelength, and the difference the difference between the experiment and simulation results tends to increase as the wavelength increases. This can be attributed to inaccuracy of refractive index data of materials at long wavelength or the small discrepancy in layer thicknesses between the actual structure and the simulation structure. Despite the small offset in peak wavelength between measurement and simulation, the variation of the peak wavelength with peak number shows consistent trend in all B-QDIP samples. The results in Fig. 6 clearly demonstrate the microcavity effect in the B-QDIP structure. Our resonant cavity enhanced B-QDIP results show that there are many possibilities to find applications of integration of IR sensors on silicon photonics platform using simple MWB and ELO processes.

To observe the microcavity effect in more detail, the bias-dependent PC spectrums of the sample C were measured, as depicted in Fig. 7. The bias-dependent PC spectrums of the as-grown QDIP and the B-QDIP are shown in Fig. 7(a) and (b), respectively. All voltage applied PC signals show the increased intensity and the same PC spectrum shape. No peak shift or change of the spectrum by applied bias was observed, indicating that the intrinsic QD characteristics are not changed. The tunneling probability of the photocurrent through the barrier is increased only by changing the bias voltage. The peak PC intensity at −2 V is 12 times higher than that at 0 V. On the other hand, the peak PC intensity at 2 V is 7.5 times higher than that at 0 V. The reverse biased PC of as-grown QDIP shows higher increment than the forward biased PC. This is due to the asymmetric structure, arising from the 40 nm of $GaAs/Al_{0.3}Ga_{0.7}As$ superlattice just right above the p-type contact layer. This superlattice was inserted in the structure as a dark current blocking layer. On the contrary, the forward biased PC of B-QDIP shows higher increment than the reverse biased PC. This is because the two QDIP structures are inverted by MWB and ELO process. This interesting behavior can also be observed in the dark current density (J) –voltage (V) characteristics. The inset of the Fig. 7(b) is J-V characteristics of the as-grown QDIP and B-QDIP of sample C. The J in forward bias region of

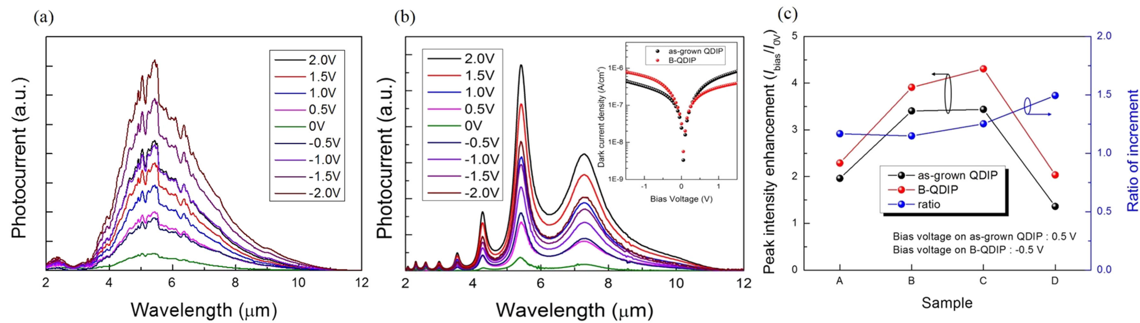

Fig. 7. (a) The PC spectra of as-grown QDIP of sample C were measured at different bias voltage from −2.0 V to 2.0 V with a step of 0.5 V. (b) The PC spectra of B-QDIP of sample C were measured at different bias voltage from −2.0 V to 2.0 V with a step of 0.5 V. The inset depicts the dark current density-voltage characteristics of as-grown QDIP and B-QDIP. (c) The peak PC intensity enhancement of QDIPs of applied bias voltage (I_{bias}) versus to 0 V (I_{0V}). The increased PC intensity value of as-grown QDIP and B-QDIP was extracted from 0.5 V and −0.5 V, respectively. The right y-axis indicates the ratio of the increment of as-grown QDIP to that of B-QDIP.

the as-grown QDIP shows almost identical current with that in reverse bias region of B-QDIP and the same trend in the other regions, showing the decalcomania characteristics of two QDIPs. The identical dark current level suggests that the material characteristics of QDs and epitaxial layers were not changed after MWB and ELO, which is also previously described in our literature [18]. Fig. 7(c) depicts the peak PC intensity enhancement of applied bias voltage (I_{bias}) versus to 0 V (I_{0V}). The increased PC intensity value of as-grown QDIP and B-QDIP were extracted from 0.5 V and −0.5 V, respectively. The right y-axis indicates the ratio of the increment, obtained by the peak PC intensity enhancement of B-QDIPs divided by that of as-grown QDIPs. All ratio of increment are greater than one, indicating that under bias condition, the PCs of B-QDIPs are more generated than those of as-grown QDIPs. This result indicates that the microcavity contributes to the increased PC. The ratio of increment shows generally marginal compared to the other cavity structure which uses a double side thick gold layer or a thick DBR layer. This is due to the low reflectivity of the only one side of thin 10 nm of gold layer. However, we believe this marginal increment can be improved by optimizing the device structure. Our resonant cavity enhanced B-QDIP results show that there are many possibilities to find applications of integration of IR sensors on silicon photonics platform using simple MWB and ELO processes.

4. Conclusion

In conclusion, the microcavity effects in the QDIP on Si substrate fabricated with MWB and ELO techniques were demonstrated. The origin of the microcavity effect of the B-QDIP was also clarified by comparing the experimental and the simulation results. To investigate the microcavity effect, four QDIP samples with different cavity length were grown and fabricated on Si substrate. All PC spectra of B-QDIPs show significantly different features from those of as-grown QDIPs. In the B-QDIPs, the resonant peaks were observed and the number of peaks increased as the cavity length increased, indicating that the resonant cavity enhanced PC. The FDTD simulation was conducted to calculate absorption spectrum for each B-QDIP structure. The absorption spectrum of the B-QDIP shows several resonance peaks as a result of the cavity structure composed of the bottom mirror of Pt/Au layer and the flat GaAs/air interface, whereas that of an as-grown QDIP shows nearly constant absorption in the simulated wavelength range. The peak wavelength of the PC spectrum and the absorption spectrum shows a good agreement, indicating the microcavity effect in the B-QDIP definitely. In addition, this microcavity contributes to increase the generation of PCs, which we confirm from the bias dependent PC measurement. The demonstrated microcavity QDIP devices are expected to find various applications in integrated chemical and bio sensors.

References

[1] S. A. Miller *et al.*, “Low-loss silicon platform for broadband mid-infrared photonics,” *Optica*, vol. 4, no. 7, pp. 707–712, 2017.
[2] A. Spott, E. J. Stanton, N. Volet, J. D. Peters, J. R. Meyer, and J. B. Bowers, “Heterogeneous integration for mid-infrared silicon photonics,” *IEEE J. Sel. Topics Quantum Electron.*, vol. 23, no. 6, Nov./Dec. 2017, Art. no. 8200810.
[3] G. Valicourt *et al.*, “Photonic integrated circuit based on hybrid III–V/silicon integration,” *J. Lightw. Technol.*, vol. 36, no. 2, pp. 265–273, Jan. 2018.
[4] J. Wu *et al.*, “Monolithically integrated InAs/GaAs quantum dot mid-infrared photodetectors on silicon substrates,” *ACS Photon.*, vol. 3, pp. 749–753, 2016.
[5] J. Huang *et al.*, “Midwave infrared quantum dot quantum cascade photodetector monolithically grown on silicon substrate,” *J. Lightw. Technol.*, vol. 36, no. 18, pp. 4033–4038, Sep. 2018.
[6] W. Chen *et al.*, “Demonstration of InAs/InGaAs/GaAs quantum dots-in-a-well mid-wave infrared photodetectors grown on silicon substrate,” *J. Lightw. Technol.*, vol. 36, no. 13, pp. 2572–2581, Jul. 2018.
[7] H. Yoshikawa, J. Kwoen, T. Doe, M. Izumi, S. Iwamoto, and Y. Arakawa, “InAs/GaAs quantum dot infrared photodetectors on on-axis Si (100) substrates,” *Electron. Lett.*, vol. 54, no. 24, pp. 1395–1397, 2018.
[8] C. W. Cheng, K. T. Shiu, N. Li, S. J. Han, L. Shi, and D. K. Sadana, “Epitaxial lift-off process for gallium arsenide substrate reuse and flexible electronics,” *Nat. Commun.*, vol. 4, 2013, Art. no. 1577.
[9] D. M. Geum *et al.*, “Ultra-high-throughput production of III–V/Si wafer for electronic and photonic applications,” *Sci. Rep.*, vol. 6, 2016, Art. no. 20610.
[10] M. S. Park, D. M. Geum, J. H. Kyhm, J. D. Song, S. H. Kim, and W. J. Choi, “InGaP/GaAs heterojunction phototransistors transferred to a Si substrate by metal wafer bonding combined with epitaxial lift-off,” *Opt. Exp.*, vol. 23 no. 21, pp. 26889–26894, 2015.
[11] M. S. Park *et al.*, “InGaAs/InP quantum well infrared photodetector integrated on Si substrate by Mo/Au metal-assisted wafer bonding,” *Opt. Mater. Exp.*, vol. 8, no. 2, pp. 413–419, 2018.
[12] T. Asano, C. Hu, Y. Zhang, M. Liu, J. C. Campbell, and A. Madhukar, “Design consideration and demonstration of resonant-cavity-enhanced quantum dot infrared photodetectors in mid-infrared wavelength regime (3-5 μm),” *IEEE J. Quantum. Electron.*, vol. 46, no. 10, pp. 1484–1491, Oct. 2010.
[13] R. S. Attaluri *et al.*, “Resonant cavity enhanced InAs/$In_{0.15}Ga_{0.85}As$ dots-in-a-well quantum dot infrared photodetector,” *J. Vac. Sci Technol. B*, vol. 25, 2007, Art. no. 1186.
[14] J. P. Kim and A. M. Sarangan, “Design and simulation of resonant cavity enhanced corrugated quantum well infrared photodetectors,” *Appl. Opt.*, vol. 45, no. 24, pp. 6065–6070, 2006.
[15] Y. N. Chen *et al.*, “Antenna-coupled microcavities for enhanced infrared photo-detection,” *Appl. Phys. Lett.*, vol. 104, 2014, Art. no. 031113.
[16] D. Palaferri, Y. Todorov, A. Mottaghizadeh, G. Frucci, G. Biasiol, and C. Sirtori, “Ultra-subwavelength resonators for high temperature high performance quantum detectors,” *New. J. Phys.*, vol. 18, 2016, Art. no. 113016.
[17] D. Palaferri *et al.*, “Room-temperature nine-μm-wavelength photo-detectors and GHz-frequency heterodyne receivers,” *Nature*, vol. 556, pp. 85–88, 2018.
[18] H. S. Kim *et al.*, “InAs/GaAs quantum dot infrared photodetector on a Si substrate by means of metal wafer bonding and epitaxial lift-off,” *Opt. Exp.*, vol. 25, no. 15, pp. 17562–17570, 2017.
[19] “FDTD Solutions,” Lumerical Inc., Vancouver, BC, Canada. [Online]. Available: http://www.lumerical.com/tcad-products/fdtd/
[20] B. Kochman *et al.*, “Absorption, carrier lifetime, and gain in InAs-GaAs quantum-dot infrared photodetectors,” *IEEE J. Quantum Electron.*, vol. 39 no. 3, pp. 459–467, Mar. 2003.
[21] J. Z. Zhang and I. Galbraith, “Intraband absorption for InAs/GaAs quantum dot infrared photodetectors,” *Appl. Phys. Lett.*, vol. 84, no. 11, pp. 1934–1936, 2004.
[22] W. G. Hu, T. Inoue, O. Kojima, and T. Kita, “Effects of absorption coefficients and intermediate-band filling in InAs/GaAs quantum dot solar cells,” *Appl. Phys. Lett.*, vol. 97, no. 19, 2010, Art. no. 193106.